



# 1 Strategic Design of Methane Observation Networks to 2 Improve Emission Estimates: A Case Study in Africa

3 Hui Li<sup>1\*</sup>, Philippe Ciais<sup>1</sup>, Frédéric Chevallier<sup>1</sup>, Bo Zheng<sup>2,3</sup>, Paul I. Palmer<sup>4</sup>, Frank Hase<sup>5</sup>,  
4 Morgan Lopez<sup>1</sup>, Elsa M Ordway<sup>6</sup>, Shushi Peng<sup>7</sup>, Danielle Monteverde<sup>8</sup>, Michel Ramonet<sup>1</sup>,  
5 Jason Michael St Clair<sup>9</sup>, Le Bienfaiteur Sagang<sup>10</sup>, Benjamin Poulter<sup>11</sup>

6 <sup>1</sup>Laboratoire des Sciences du Climat et de l'Environnement, LSCE/IPSL, CEA-CNRS-UVSQ, Université  
7 Paris-Saclay, F-91191 Gif-sur-Yvette, France.

8 <sup>2</sup>Shenzhen Key Laboratory of Ecological Remediation and Carbon Sequestration, Institute of Environment  
9 and Ecology, Tsinghua Shenzhen International Graduate School, Tsinghua University, Shenzhen 518055,  
10 China.

11 <sup>3</sup>State Environmental Protection Key Laboratory of Sources and Control of Air Pollution Complex, Beijing  
12 100084, China.

13 <sup>4</sup>National Centre for Earth Observation, University of Edinburgh, Edinburgh, EH9 3FF, UK.

14 <sup>5</sup>Institute of Meteorology and Climate Research (IMK-ASF), Karlsruhe Institute of Technology (KIT), 76344  
15 Eggenstein-Leopoldshafen, Germany.

16 <sup>6</sup>Department of Ecology and Evolutionary Biology and Institute of the Environment and Sustainability,  
17 University of California, Los Angeles, Los Angeles, California, USA.

18 <sup>7</sup>Institute of Carbon Neutrality, Sino-French Institute for Earth System Science, College of Urban and  
19 Environmental Sciences, and Laboratory for Earth Surface Processes, Peking University, Beijing, China.

20 <sup>8</sup>Spark Climate Solutions, Covina, CA, 91723, USA.

21 <sup>9</sup>NASA Goddard Space Flight Center, Greenbelt, MD, USA.

22 <sup>10</sup>Institute of the Environment and Sustainability, University of California, Los Angeles, Los Angeles, CA,  
23 USA.

24 <sup>11</sup>Spark Climate Solutions, San Francisco, CA, USA.

25 *Correspondence to:* Hui Li (hui.li@lsce.ipsl.fr)

26 **Abstract.** Ground-based and satellite atmospheric observations are essential for reducing uncertainties in  
27 methane (CH<sub>4</sub>) emissions by atmospheric inversion, particularly in data-sparse regions such as Africa.  
28 However, adding new observation sites does not yield linear improvements of emission uncertainties because  
29 overlapping transport sensitivities reduces marginal information gain. Here we develop a Bayesian  
30 framework to strategically optimize CH<sub>4</sub> observation network design for column retrievals from upward-  
31 looking Fourier Transform Infrared (FTIR) spectrometers (e.g., EM27/SUN), jointly identifying the optimal  
32 number of sites and their spatial configuration. The framework quantifies uncertainty reduction for grid-point  
33 (1°) total and sectoral emissions while accounting for transport redundancy, cloud screening, and  
34 observational errors. Using January and July as representative months, we find that uncertainty reduction  
35 increases rapidly during early network expansion but gradually saturates beyond a certain number of  
36 additional sites. An optimized configuration of ten new sites added to the existing network achieves over 65%  
37 reduction in prior uncertainty for total African CH<sub>4</sub> emissions in both months, with comparable improvements



38 across fire, wetland, and anthropogenic sectors. Sensitivity analyses indicate that while the optimal number  
39 of sites varies with assumptions about cloud filtering, the spatial configuration remains robust, supporting  
40 cost-effective observation network design in data-sparse regions.

## 41 **1. Introduction**

42 Methane (CH<sub>4</sub>) emissions from Africa play a critical role in the global CH<sub>4</sub> budget, accounting for  
43 approximately 14–16% of global emissions during 2000–2019 (Saunois et al., 2025; Lunt et al., 2019; Ernst  
44 et al., 2024). Beyond being a major emitting region over the last two decades, Africa has emerged as a  
45 dominant contributor to the recent spike of the global CH<sub>4</sub> emission growth rate, contributing nearly 50% of  
46 the global emission increase in recent years (Qu et al., 2022; Feng et al., 2023). This rise has been largely  
47 attributed to enhanced wetland emissions linked to intensifying rainfall and hydroclimatic variability,  
48 particularly given the region’s high vulnerability to climate change (Gunaratne et al., 2025; Helfter et al.,  
49 2021). The potential for rapid socio-economic development and land-use change in Africa in the coming  
50 decades further elevates the region’s importance in the global CH<sub>4</sub> budget (Ernst et al., 2024). Despite this  
51 growing significance, African methane emissions remain among the most uncertain of all major source  
52 regions (Saunois et al., 2025). These large uncertainties arise not only from bottom-up inventories, where  
53 activity data and emission factors are often incomplete or poorly constrained, but also from top-down  
54 inversion approaches that rely on atmospheric observations (Mostefaoui et al., 2024). In Africa, the  
55 effectiveness of atmospheric inversions is severely limited by the scarcity of observational constraints  
56 (Valentini et al., 2014; Ciaï et al., 2011). Although satellite observations provide valuable large-scale  
57 coverage, their ability to accurately constrain African CH<sub>4</sub> emission estimates is hindered by overhead cloud  
58 cover, surface reflectance variability, and limited opportunities for independent validation (Mengistu and  
59 Mengistu Tsidu, 2020; Western et al., 2021; Cressot et al., 2016). Yet, ground-based measurements needed  
60 to calibrate, validate, and compensate for gaps in satellite observations are especially sparse in Africa  
61 (Merbold et al., 2021; Gaubert et al., 2023). The Total Carbon Column Observing Network (TCCON)  
62 currently includes only four sites (Ascension, Izaña, La Réunion, and Nicosia) with partial African coverage  
63 (Wunch et al., 2011), which are located on surrounding islands, offering limited sensitivity to major inland  
64 emission hotspots, particularly across Central Africa (discussed in Section 3.1).

65 Previous studies made the case that strengthening ground-based atmospheric observations can substantially  
66 reduce posterior uncertainties in atmospheric inversions, as illustrated by the dense observation networks in  
67 Europe, North America, and China (Kadygrov et al., 2015; Palmer et al., 2019; Ganesan et al., 2015; Zhang  
68 et al., 2022). These networks typically combine multiple observing systems, including tall towers that provide  
69 continuous, high-precision measurements of CH<sub>4</sub> and other trace gases in the planetary boundary layer, and  
70 aircraft profiles that sample vertical concentration gradients over regional scales (Sasakawa et al., 2010;  
71 Adame et al., 2024; Sweeney et al., 2022; Liu et al., 2025). While these dense networks should offer strong  
72 constraints, they require substantial infrastructure, logistical support, and long-term maintenance, making



73 their deployment particularly challenging in remote regions. As a lower-cost alternative, EM27/SUN Fourier  
74 Transform Infrared (FTIR) spectrometers have been increasingly used for ground-based column retrievals of  
75 greenhouse gases (such as CO<sub>2</sub> and CH<sub>4</sub>) (Hase et al., 2016; Humpage et al., 2024; Park et al., 2024). Unlike  
76 tall tower measurements that mainly capture near-surface concentrations, column observations integrate  
77 signals over a deeper tropospheric layer and are therefore representative of broader regional footprints  
78 (Keppel-Aleks et al., 2013). EM27/SUN instruments are portable, require relatively limited infrastructure  
79 and maintenance, and can be deployed in regions where tall towers or aircraft operations would be impractical  
80 or extremely costly (Frey et al., 2019). However, EM27/SUN have limitations, including retrievals restricted  
81 to daytime and clear-sky conditions, and the need for careful inter-calibration to ensure network consistency.  
82 Despite these constraints, recent studies have demonstrated that EM27/SUN-based networks can effectively  
83 enhance observational constraints and reduce posterior uncertainties in atmospheric inversions (Alberti et al.,  
84 2022; Kurganskiy et al., 2025; Zhou et al., 2025). Accordingly, the column-average dry-air mole fraction of  
85 CH<sub>4</sub> (XCH<sub>4</sub>) is adopted as the assumed observed variable in this study, with EM27/SUN as the default  
86 observation platform. This configuration drives our network design framework.

87 Importantly, simply increasing the number of observation sites is neither scientifically optimal nor  
88 economically feasible (Nickless et al., 2020a). As station density increases, the observation footprints of  
89 concentrations to the emissions to be retrieved increasingly overlap, leading to diminishing marginal  
90 information gain due to redundant transport sensitivities (Kadygrov et al., 2015). Given the costs associated  
91 with station deployment, operation, and maintenance, an optimized cost-effective observing strategy is  
92 required to balance uncertainty reduction against observational redundancy and resource constraints  
93 (Merbold et al., 2021). Information-based network design approaches within Bayesian inversion frameworks  
94 have been developed to address this challenge (Kaminski and Rayner, 2017). These methods quantify  
95 posterior uncertainty reduction under alternative observing configurations and have been applied at regional  
96 scales to evaluate station placement and prior error sensitivity (Merbold et al., 2021). However, most existing  
97 studies focus on configuration ranking of tall-tower networks, particularly in the case of Africa (Nickless et  
98 al., 2020b; Lauvaux et al., 2012), whereas spatial optimization of FTIR column networks under cloud  
99 constraints remains limited.

100 Here, we use the African continent, a region with enormous observational gaps, as a case study to develop a  
101 systematic framework for optimal XCH<sub>4</sub> atmospheric observation network design. The proposed framework  
102 is built upon a Bayesian approach that strategically and explicitly quantifies uncertainty reduction under  
103 incremental network expansion, allowing both the optimal number of stations and their spatial configuration  
104 to be identified. Determining the optimal network size provides an evidence-based approach for proposing a  
105 realistic number of new stations from a large set of potential candidates, before selecting the most effective  
106 spatial configuration. By accounting for footprint (i.e., atmospheric transport) overlap, cloud-related  
107 observational limitations, and sector-specific emission characteristics, the framework provides quantitative  
108 guidance for cost-effective network design. Sensitivity experiments further demonstrate that while the  
109 optimal number of sites responds to assumptions about cloud effects, the resulting spatial configuration of



110 optimized sites is robust across a certain range of parameter settings, underscoring the reliability of the  
111 proposed approach.

## 112 2. Materials and methods

113 This section describes the methodological framework developed to evaluate and optimize a future XCH<sub>4</sub>  
114 observation network over Africa, focusing on observing and quantifying CH<sub>4</sub> emissions. The framework is  
115 designed to quantify how atmospheric observations reduce emission uncertainty and to identify cost-effective  
116 network designs under certain observational constraints. The analysis focuses on January and July 2025,  
117 which represent two contrasting meteorological regimes and emission backgrounds over the African  
118 continent. These two periods are selected to capture the seasonal variability of CH<sub>4</sub> sources and atmospheric  
119 transport that is critical for network design. Section 2.1 introduces the Bayesian inversion principles used to  
120 quantify the emission uncertainty reduction, including the formulation of the prior error covariance matrix  
121 and the representation of atmospheric transport sensitivities. Section 2.2 presents the strategic Bayesian  
122 network design framework developed to efficiently determine both the optimal number of new observation  
123 sites and their spatial configuration. Section 2.3 assesses the influence of the assumed spatial error correlation  
124 length on posterior variance reduction. Section 2.4 describes the treatment of cloud fraction and its  
125 incorporation into observational constraints. The notation in this paper follows Rayner et al. (2019), where  
126 uppercase bold symbols denote matrices and lowercase bold symbols denote vectors.

### 127 2.1 Bayesian algorithms

128 The impact of atmospheric observations on CH<sub>4</sub> emission estimates is quantified using a Bayesian inversion  
129 framework, in which prior information on monthly gridded surface emissions is updated by observational  
130 constraints through atmospheric transport modelling. The Kalman gain matrix (**K**) determines the relative  
131 influence of observations and prior information in the posterior update (Rodgers, 2000; Rayner et al., 2019):

$$132 \quad \mathbf{K} = \mathbf{B}\mathbf{H}^T (\mathbf{H}\mathbf{B}\mathbf{H}^T + \mathbf{R})^{-1} \quad (1)$$

133 where **B** denotes the prior emission error covariance matrix, **H** is the Jacobian matrix (also known as footprint  
134 or transport sensitivity) linking surface emissions to XCH<sub>4</sub> observations, **R** is the observational error  
135 covariance matrix. The observational error covariance **R** is prescribed as diagonal, with a constant standard  
136 deviation of 5 parts per billion (ppb) as the default value, consistent with the expected retrieval precision of  
137 EM27/SUN spectrometers (Doc et al., 2025). Doing this, we neglect the contributions of **H** (i.e., the model  
138 error) and of the sub-monthly and sub-pixel emission variability (i.e., the aggregation error) in the error  
139 budget.

140 In this study, the prior uncertainty for each grid cell is defined as 150% of the maximum value of the prior  
141 emissions among the eight nearest neighboring grid cells for the corresponding month. The scaling factor  
142 adopted here (150%) is slightly higher than values used in previous studies (e.g., 120%) (Cressot et al., 2014),



143 in order to account for the higher spatial resolution and the limited number of emission inventories applied  
144 in this work. Four emission categories include total (sum of anthropogenic and natural sources), fire, wetlands,  
145 and anthropogenic CH<sub>4</sub> (data sources are listed in Table S1) (Van Der Werf et al., 2025; Van Der Werf et al.,  
146 2017; Kaiser et al., 2012; McDuffie et al., 2020; Crippa et al., 2024). The number of adopted inventories is  
147 limited (three datasets for fire and anthropogenic emissions, and four for wetlands, seen in Table S1). While  
148 this may influence the exact optimized configurations under the prescribed prior, it does not fundamentally  
149 affect the framework performance. As shown in Section 3.4, the test with spatially perturbed prior fields  
150 demonstrate that the framework adaptively adjusts site layouts in response to changes in prior spatial structure.  
151 All prior data are acquired for the year 2023, representing the most up-to-date ensemble of different emission  
152 inventories currently available. The fact that the reference year for the inventories (2023) differs from that of  
153 the meteorology (2025) may affect specific site placements but does not alter the methodological validity of  
154 the optimization framework, which is independent of absolute timing. All prior monthly emission fields are  
155 first regridded to a common 1° × 1° grid to ensure consistency with **H** and then the uncertainties are estimated.  
156 The prior error covariance matrix is constructed as:

$$157 \quad \mathbf{B} = \mathbf{dCd}^T \quad (2)$$

158 where **d** is a vector of gridded 1σ prior uncertainties, and **C** is a spatial correlation matrix. Spatial correlations  
159 C<sub>ij</sub> between grid cells *i* and *j* are represented using an exponential decay function:

$$160 \quad C_{ij} = \exp\left(-\frac{d_{ij}}{l}\right) \quad (3)$$

161 where *d<sub>ij</sub>* is the distance between grid cells *i* and *j* on the sphere. A land–sea mask is applied to prevent  
162 correlations between land and ocean grid cells, and a horizontal correlation length scale of 500 km is assumed  
163 over land and ocean. The sensitivity analyses to determine this value are detailed in Section 2.3. The resulting  
164 covariance matrix **B** is constructed separately for each target month and emission sector at 1° resolution. The  
165 resulting uncertainty budgets are comparable to those reported in previous studies (Fig. S1), as discussed in  
166 Section 2.3.

167 Transport sensitivities (**H**) are derived from adjoint simulations of the LMDZ model (Hourdin et al., 2020)  
168 in January and July 2025, run globally at approximately 90 km horizontal resolution using a hexagonal grid  
169 and 79 vertical layers. This relatively high resolution for a global transport model allows realistic  
170 representation of regional transport patterns while avoiding the need for lateral boundary conditions required  
171 by regional models. For simplicity, we assume that the observations are directly XCH<sub>4</sub>, without any specific  
172 averaging kernel and associated retrieval prior profile. Chemical loss processes are neglected, as the analysis  
173 focuses on a within-month timescale. Flux sensitivities are reprojected onto the 1° grid within **H** using the  
174 adjoint of a mass-conserving flux interpolation, ensuring consistency between the inversion control vector  
175 and the sensitivity matrix. Details of the LMDZ hexagonal-grid simulations are provided in Chevallier et al.  
176 (2025). This model is run for full calendar months. In order to avoid running the adjoint over more than one



177 calendar month at a time, we take only XCH<sub>4</sub> observations into account during the second half of the month.  
178 Thus, the sensitivity of the earliest observation of a month to surface fluxes from previous months is assumed  
179 to be sufficiently diluted so as not to significantly improve knowledge of African emissions. Observations at  
180 each site are simulated once per day at local noon, and the adjoint model is integrated backward to the first  
181 day of the same month, resulting in backward integration lengths ranging from 16 to 30 days depending on  
182 the month. Examples of site-specific footprint sensitivities are shown in Fig. S2. The posterior error  
183 covariance matrix **A** is given by:

$$184 \quad \mathbf{A} = \mathbf{B} - \mathbf{KHB} \quad (4)$$

185 and the relative reduction in uncertainty brought by these observations can be expressed as:

$$186 \quad \mathbf{I} - \mathbf{AB}^{-1} = \mathbf{KH} \quad (5)$$

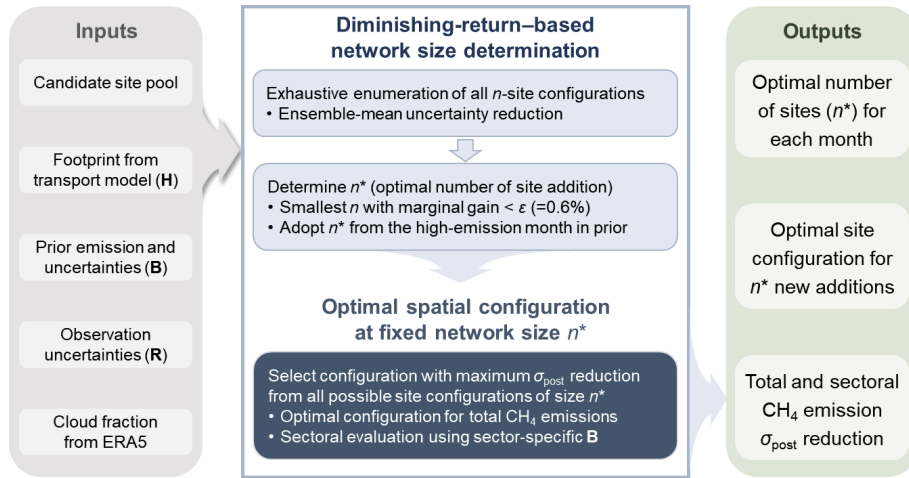
187 In this study, posterior uncertainty reduction relative to the prior is used as the primary metric to evaluate  
188 and compare different observation network configurations. It is important to note that the uncertainty  
189 reductions reported here should be interpreted as a proxy for the potential information gain achievable by an  
190 optimized network, rather than as a direct prediction of operational inversion performance. This is partly due  
191 to simplifying assumptions adopted for network design purposes, including the use of transport sensitivities  
192 derived from half-month adjoint integrations and prescribed, spatially uniform observation uncertainties.

## 193 **2.2 A strategic Bayesian network design framework**

194 Building on the Bayesian inversion framework described above, we develop a strategic Bayesian network  
195 design framework to optimize XCH<sub>4</sub> observation networks of new FTIR instruments beyond the existing six  
196 stations surrounding Africa and the three in Ivory Coast, Namibia, and shore of Lake Victoria. Among these  
197 operational sites, four (Ascension, Izaña, La Réunion, and Nicosia) belong to the TCCON network, which  
198 operates high-resolution FTIR spectrometers (typically Bruker Optik GmbH IFS 125HR FTS) (Pollard et al.,  
199 2021), whereas the remaining stations use lower-cost EM27/SUN instruments. Three of these stations  
200 (LAMTO, AMV, and Amsterdam Island) are operated by the Laboratory for Climate and Environmental  
201 Sciences (LSCE), one (Gobabeb) by the Karlsruhe Institute of Technology (KIT), and one (Jinja) by the  
202 University of Leicester (Table S2). The framework quantifies how posterior uncertainty in African CH<sub>4</sub>  
203 emissions responds to incremental network expansion and identifies an optimal balance between information  
204 gain and network size. The optimization assumes a predefined candidate site pool reflecting practical  
205 deployment constraints. For the African case study, the pool consists of nine existing stations, predominantly  
206 located along the continental periphery, four planned African sites outside the current operational network,  
207 and 21 additional candidate sites, yielding 34 potential locations in total (Table S2). The 21 additional  
208 candidate sites were determined based on a combination of areas with high prior emission estimates across  
209 Africa and locations that have high potential for deploying EM27/SUN instruments (e.g., existing local  
210 research institutions or field stations capable of supporting and maintaining this equipment). The nine  
211 operational and four planned African sites are treated as a fixed baseline network, while the remaining



212 candidate sites are considered for incremental expansion. The framework simultaneously determines the  
 213 optimal number of additional observation sites based on uncertainty-reduction efficiency and identifies the  
 214 spatial configuration of sites that minimizes posterior uncertainty at the prescribed network size using  
 215 Bayesian evaluation.



216

217 **Figure 1. The Bayesian network design framework for atmospheric XCH<sub>4</sub> observations.** The parameter  
 218 explanation and default settings are listed in Table S3.

219 This system first quantifies how posterior uncertainty in spatially integrated African CH<sub>4</sub> emissions decreases  
 220 as additional observation sites are introduced, with the goal of determining an efficient network size prior to  
 221 optimizing the exact site locations. Let  $\mathbf{x} \in \mathbb{R}^N$  denote the gridded emission state vector. The target quantity  
 222 is defined as a linear functional of the state:

$$223 \quad y = \mathbf{1}^T \mathbf{x} \quad (6)$$

224 where  $\mathbf{1}$  is an aggregation vector (i.e., grid emissions in Africa). The corresponding prior uncertainty is  
 225 obtained by applying this operator to the prior covariance  $\mathbf{B}$ :

$$226 \quad \sigma_{prior}^2 = \mathbf{1}^T \mathbf{B} \mathbf{1} \quad (7)$$

227 For a given network configuration  $c$ , we construct the observation operator  $\mathbf{H}_c$  by stacking all available daily  
 228 column sensitivities from the base network plus the selected candidate sites after cloud filtering, and compute  
 229 the posterior covariance  $\mathbf{A}_c$  following the Bayesian update described in Section 2.1,

$$230 \quad \mathbf{A}_c = \mathbf{B} - \mathbf{B} \mathbf{H}_c^T (\mathbf{H}_c \mathbf{B} \mathbf{H}_c^T + \mathbf{R})^{-1} \mathbf{H}_c \mathbf{B} \quad (8)$$

231 The posterior uncertainty of the same aggregated quantity is then estimated:

$$232 \quad \sigma_{post}^2 = \mathbf{1}^T \mathbf{A}_c \mathbf{1} \quad (9)$$



233 We then quantify the information gain for configuration  $c$  using the relative uncertainty reduction  $r(c)$ :

$$234 \quad r(c) = 1 - \frac{\sigma_{post}(c)}{\sigma_{prior}} \quad (10)$$

235 For each candidate number of additional site  $n$ , we evaluate an ensemble of configurations formed by  
236 combining the fixed base network with all (exhaustively enumerated)  $n$ -site subsets from the candidate pool.  
237 This yields an ensemble of  $\sigma_{post}(c)$  and thus  $r(c)$  values that reflects both transport-sensitivity overlap and  
238 cloud-driven data availability constraints. The ensemble-mean uncertainty reduction at network size  $n$  is  
239 denoted as  $P(n)$ :

$$240 \quad P(n) = \frac{1}{C_n} \sum_{c \in C_n} 1 - \frac{\sigma_{post}(c)}{\sigma_{prior}} \quad (11)$$

241 We summarize network-size performance by the ensemble-mean reduction. The optimal number of  
242 additional sites  $n^*$  determined using a diminishing-return criterion:  $n^*$  is the smallest  $n$  for which the relative  
243 marginal gain ( $\Delta P(n) = (P(n) - P(n-1)) / P(n-1)$ ) falls below a prescribed threshold  $\epsilon = 0.6\%$ , corresponding to a  
244  $0.6\%$  additional reduction per added site (sensitivity tests shown in Section 3.4).

245 Given the optimal network size  $n^*$ , the optimal configuration is selected from the ensemble of configurations  
246 with  $n = n^*$  as the one that provides the largest uncertainty reduction in total African  $\text{CH}_4$  emissions. Sector-  
247 specific uncertainty reductions are subsequently evaluated by applying sectoral prior covariance matrices  $\mathbf{B}$ ,  
248 while retaining the same transport sensitivities  $\mathbf{H}$ . Differences in uncertainty reduction across sectors  
249 therefore primarily reflect contrasts in prior uncertainty structures rather than transport sensitivities.

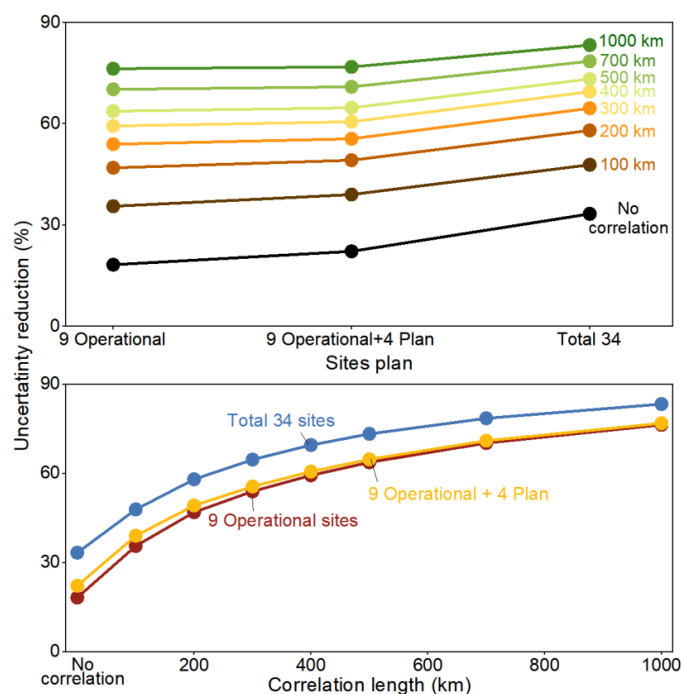
### 250 **2.3 The impact of assumed prior error correlation length on uncertainty reduction**

251 The horizontal correlation length determines how prior emission errors are spatially coupled in the covariance  
252 matrix  $\mathbf{B}$ . In simple terms, it controls how strongly emission errors in one grid cell are assumed to be  
253 correlated with those in neighboring cells. A larger correlation length implies that flux corrections inferred  
254 at one location can spread over a broader surrounding region, effectively distributing observational  
255 information across larger spatial scales. This generally leads to more optimistic large-scale uncertainty  
256 reduction, whereas shorter correlation lengths confine corrections to local scales and yield more conservative  
257 reductions. To assess the sensitivity of our results to this assumption, we conducted experiments with  
258 correlation lengths ranging from no spatial correlation to 1000 km (Fig. 2). Posterior uncertainty reduction  
259 increases substantially with larger correlation lengths. For example, the reduction achieved by the existing  
260 nine operational sites rises from 18% under no correlation to 76% at 1000 km. This increase is nonlinear and  
261 gradually saturates, with a clear flattening beyond approximately 500 km. We therefore adopt 500 km as the  
262 default value, representing a pragmatic compromise between local and large-scale coupling. Under this  
263 assumption, the resulting global prior uncertainty budget is approximately  $88 \text{ Tg yr}^{-1}$  ( $\sim 17\%$ ) (Fig. S1), which  
264 is close to the  $\sim 18\%$  global uncertainty reported by Saunois et al. (2025). Regional uncertainty budgets over



265 Africa are estimated to range between 33% and 50%, which fall within, though slightly below, the broader  
 266 range of 31–90%. These comparisons suggest that the magnitude of the prescribed prior uncertainties is  
 267 broadly consistent with current global methane budget assessments.

268 At present, the lack of dense biogeochemical in situ flux observations over Africa prevents an empirical  
 269 constraint on spatial error correlations. The adopted length scale should thus be regarded as a structural  
 270 assumption rather than a directly observed quantity. Given the strong spatial heterogeneity of wetland  
 271 emissions, true correlations likely vary across regions and seasons. While the assumed correlation length  
 272 substantially affects the absolute magnitude of posterior uncertainty reduction, it has limited influence on the  
 273 relative ranking of network configurations. The incremental gains from adding new sites remain consistent  
 274 across the tested range, indicating that the optimization results are robust to reasonable variations in this  
 275 parameter.



276

277 **Figure 2. The impact of assumed prior error correlation length on uncertainty reduction.** Tests on three  
 278 basic site plans, including 9 operational sites only, 9 operational and 4 planned sites, and a network with total  
 279 34 sites.

#### 280 2.4 The impact of clouds on uncertainty reduction estimation

281 Cloud conditions strongly influence the effectiveness of ground-based XCH<sub>4</sub> observations by limiting both  
 282 data availability and the sensitivity of column observations to surface emissions. Cloud cover reduces the  
 283 number of valid retrievals and weakens the effective constraint that individual stations can provide on surface  
 284 fluxes (Choudhury and Goren, 2025). To explicitly account for this effect, cloud screening is directly



285 incorporated into the construction of the observational sensitivity matrix  $\mathbf{H}$ . Hourly total cloud cover (TCC)  
286 fields from the fifth generation ECMWF reanalysis for the global climate and weather (ERA5) (Hersbach et  
287 al., 2020) are used for January and July 2025. For each baseline and candidate observation site, cloud fraction  
288 is extracted from the nearest ERA5 grid cell. Daily cloud statistics are derived from hourly values. Under the  
289 default settings, a day is classified as cloud-contaminated and excluded if more than 10% of the hourly  
290 records (minimum valid fraction in Table S3) exceed a cloud fraction (CF) threshold of 0.5. This conservative  
291 screening is applied to the latter 15 days of each month, corresponding to the period over which transport  
292 footprints are simulated. Only days passing the cloud filter are retained, and their corresponding footprints  
293 are included as individual rows in the sensitivity matrix  $\mathbf{H}$ . Cloud-contaminated days are excluded entirely,  
294 effectively reducing the number of observational constraints associated with a given station.

295 Cloud screening affects the inversion by modifying the effective sensitivity matrix  $\mathbf{H}$ . By reducing the  
296 number of valid observations and altering their temporal sampling, cloud filtering decreases the available  
297 information content and limits the achievable posterior uncertainty reduction for individual sites. Embedding  
298 cloud screening directly into the construction of  $\mathbf{H}$  therefore allows the framework to account for more  
299 realistic observational availability and prevents overestimation of the constraint provided by candidate  
300 stations. This treatment also contributes to the diminishing marginal returns observed when adding sites in  
301 regions with frequent cloud cover, ensuring that the optimized network design reflects both atmospheric  
302 transport sensitivity and practical observing conditions. To assess the robustness of the network design,  
303 sensitivity experiments are conducted by varying key cloud-related parameters, together with additional tests  
304 of other major system parameters (14 experiments in total; see Section 3.4).

### 305 3. Results

#### 306 3.1 Overview of current EM27/SUN site deployment in Africa

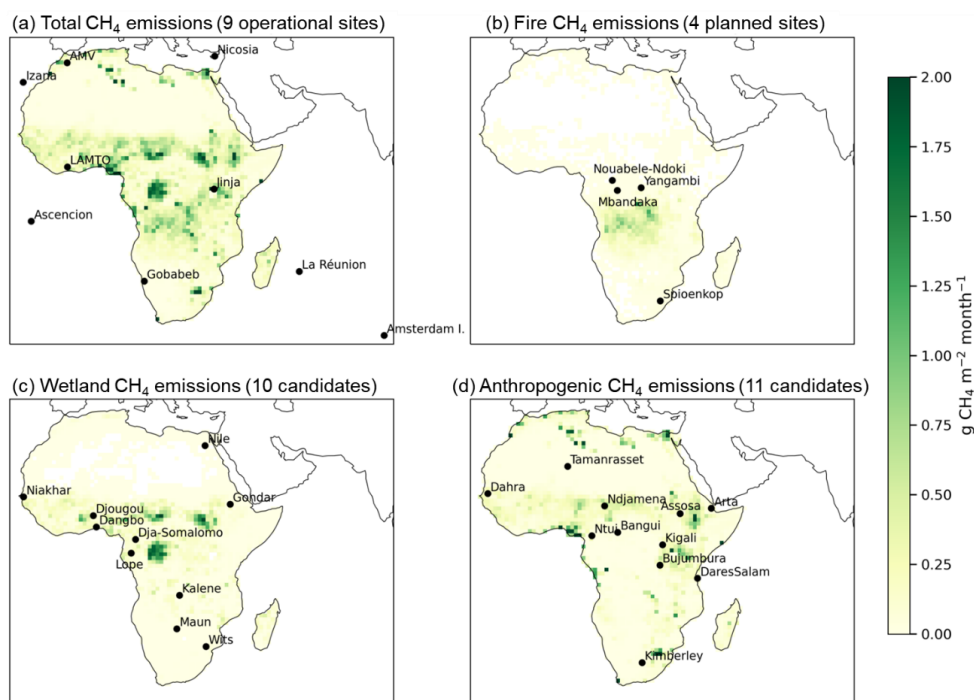
307 African  $\text{CH}_4$  emissions exhibit strong spatial heterogeneity across sectors, with anthropogenic and wetland  
308 sources dominating the continental total and fire emissions contributing more episodically and regionally  
309 (Figs. 3 and S3). In January, anthropogenic sources account for 57.9% of total African  $\text{CH}_4$  emissions,  
310 followed by wetland (31.5%) and fire (10.6%). In July, the corresponding contributions are 52.6%, 32.3%,  
311 and 15.1%, respectively (Fig. S4). Anthropogenic emissions exhibit a relatively stable spatial pattern across  
312 months, with pronounced hotspots over the Gulf of Guinea, the Nile Delta, and parts of South Africa,  
313 reflecting a spatially fragmented and regionally clustered structure (Mostefaoui et al., 2024). Wetland  
314 emissions show broadly similar mean spatial patterns in both months, with strong clustering over Central  
315 Africa, particularly around the Cuvette Centrale peatland complex in the Congo Basin, a well-recognized  
316 hotspot of tropical  $\text{CH}_4$  emissions (Lunt et al., 2019; Barthel et al., 2022; Xiao et al., 2024). In contrast, fire  
317 emissions display pronounced seasonal shifts, concentrating mainly in southern Africa in July and in Central  
318 Africa in January, consistent with previous studies (Van Der Velde et al., 2024; Eames et al., 2025). Across  
319 the inventories adopted as priors in this study, biogenic sources exhibit substantially greater variability



320 despite the limited number of available inventories. Fire and wetland CH<sub>4</sub> emissions show mean coefficients  
321 of variation (CV) of 84% and 127%, respectively, whereas anthropogenic emissions exhibit a much smaller  
322 CV of 22% (Fig. S5). This pronounced inter-inventory spread underscores the considerable uncertainty  
323 associated with biogenic sources and highlights the need for improved observational constraints, particularly  
324 for Africa where natural sources contribute a substantial fraction of total methane emissions.

325 Against this emission context, we first quantify the constraint provided by the existing observing network.  
326 The nine operational sites alone (Fig. 3a) reduce the posterior uncertainty of total African CH<sub>4</sub> emissions by  
327 62% in January and 64% in July (Fig. S6). It is important to note that the absolute magnitude of posterior  
328 uncertainty reduction depends on prior error assumptions (Fig. 2) and should therefore be interpreted  
329 primarily as a comparative reference metric. The substantial reduction obtained from only nine sites thus  
330 reflects posterior covariance changes under assumed error structures rather than real-world inversion  
331 accuracy. Incorporating the four planned African EM27/SUN sites (Yangambi, Mbandaka, Nouabalé-Ndoki,  
332 and Spioenkop) outside the current operational network (dots in Fig. 3b) yields marginal additional reductions,  
333 reaching 63% in January and 65% in July (Fig. S6). Three of these stations are located within the Congo  
334 Basin region, forming a dense cluster in Central Africa, while the fourth is situated in southern Africa. The  
335 three central African sites therefore sample broadly similar emission regions. In addition, regional wind fields  
336 organize coherent transport pathways across the Congo Basin, while high convective available potential  
337 energy (CAPE) promotes strong vertical mixing (Fig. S7). Together, these atmospheric conditions lead  
338 nearby stations to experience similar upwind sensitivities, resulting in substantial overlap in transport  
339 footprints (Figs. S2b and S2d).

340 To assess the upper bound of the achievable constraints, we consider an idealized scenario in which all  
341 candidate sites are simultaneously deployed. Under this configuration, uncertainty reduction reaches 71%  
342 and 73% in January and July, respectively (Fig. S6), yet the improvement relative to the current network is  
343 clearly sublinear (see Section 3.2). As site density increases, transport footprints increasingly overlap (Fig.  
344 S2), particularly along dominant seasonal flow structures such as the cross-equatorial pathway in January  
345 and the West African monsoon corridor in July (Fig. S7). These organized circulation regimes channel air  
346 masses through similar regions, causing additional sites to sample correlated source areas and thereby  
347 limiting incremental information gain. Cloud-related data loss further constrains the effectiveness of the  
348 network to constrain emissions within the convective Intertropical Convergence Zone (ITCZ), including the  
349 southern Congo Basin in January and the Sahelian belt in July (Fig. S7). Together, these results demonstrate  
350 that simply increasing the number of observation sites does not guarantee proportional improvements in CH<sub>4</sub>  
351 emission constraints. Instead, the strong nonlinearity between network size and uncertainty reduction  
352 underscores the need to jointly optimize both the number of additional sites and their spatial configuration to  
353 achieve cost-effective network design.



354

355 **Figure 3. Sectoral CH<sub>4</sub> emissions and observation coverage over Africa in July.** (a) total CH<sub>4</sub> emissions  
 356 with the current nine operational sites (La Réunion, Nicosia, Ascension, Izaña, LAMTO, AMV, Gobabeb,  
 357 Jinja, Amsterdam Island); (b) fire CH<sub>4</sub> emissions with four planned observation sites (Yangambi, Mbandaka,  
 358 Nouabele-Ndoki, Spioenkop); (c) wetland CH<sub>4</sub> emissions with ten candidate sites (Dja-Somalomo, Wits,  
 359 Niakhar, Nile, Djougou, Dangbo, Kalene, Gondar, Lope, Maun); and (d) anthropogenic CH<sub>4</sub> emissions with  
 360 the remaining eleven candidate sites (Dahra, Ntuli, Kigali, Bujumbura, Arta, Assosa, Bangui, Kimberley,  
 361 Tamanrasset, Ndjamena, DaresSalam). The same plot for January is shown in Fig. S3. Emission background  
 362 outside Africa has been masked for clarity.

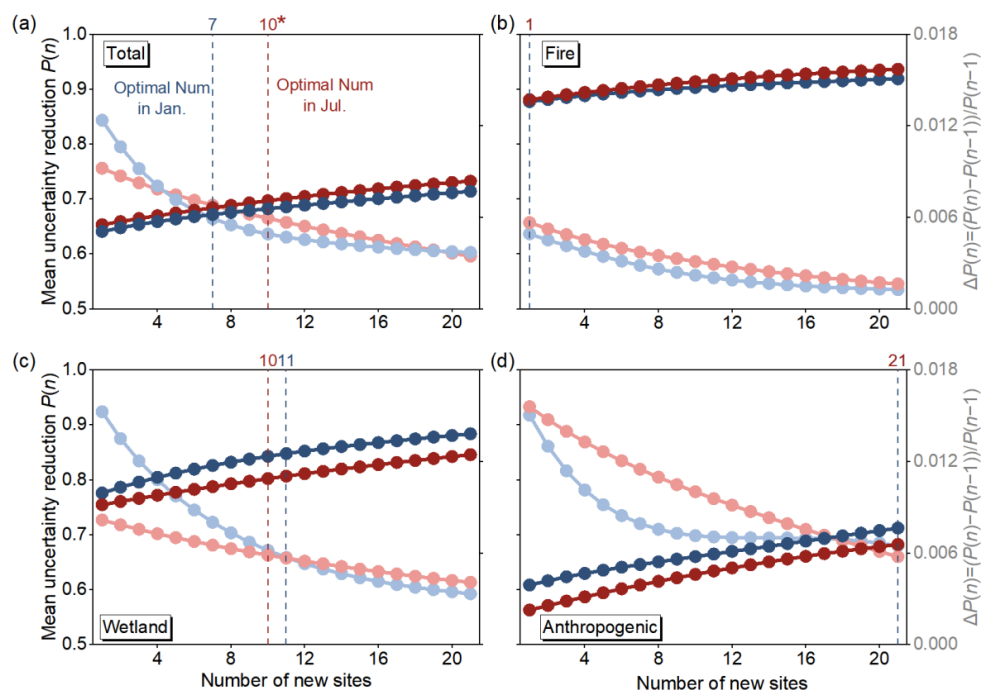
### 363 3.2 Optimal number of new observation sites

364 As the number of observation sites increases, the uncertainty reduction exhibits a clear diminishing-return  
 365 behavior across all emission sectors (Fig. 4). For both total and sectoral CH<sub>4</sub> emissions, the ensemble-mean  
 366 uncertainty reduction  $P(n)$  increases when a small number of sites are added, but progressively saturates as  
 367 additional sites provide increasingly redundant information due to overlapping transport sensitivities.  
 368 Correspondingly, the relative marginal gain  $\Delta P(n)$  decreases monotonically with increasing network size,  
 369 providing an objective criterion for identifying an optimal number of new stations. This behavior is  
 370 consistently observed for total, fire, wetland, and anthropogenic emissions, confirming that diminishing  
 371 returns are an intrinsic feature of network expansion rather than an artifact of sector-specific prior  
 372 assumptions. It is important to note that the sector-specific experiments vary only the prior covariance (**B**),  
 373 with identical transport sensitivities (**H**), and are designed to diagnose how source heterogeneity affects  
 374 network-size requirements, rather than to imply perfect sector separability in real-world inversions, where  
 375 sources are spatially mixed and attribution remains prior-dependent.



376 Despite this common pattern, the optimal number of additional sites required to satisfy the marginal gain  
377 criterion ( $\varepsilon=0.6\%$  in default setting) varies across sectors and between months (Fig. 4), reflecting differences  
378 in the spatial heterogeneity and seasonal redistribution of emission sources. Fire emissions require the fewest  
379 additional sites, with a single new site sufficient in January and July, respectively, to reach the threshold.  
380 This reflects the strong spatial clustering of African fire activity, concentrated in the Sahel–Sudan belt during  
381 boreal winter and in the southern miombo woodlands and savannas during boreal summer, which are already  
382 well covered by the four planned stations (Figs. 4b and S3b). Wetland emissions require 11 new sites in  
383 January and 10 in July. Although their mean emissions are strongly concentrated over Central Africa,  
384 seasonal variability extends across large parts of the continent, with increases and decreases spanning both  
385 northern and southern Africa (Fig. S8c). Capturing this widespread variability therefore requires a larger  
386 number of observing sites. In contrast, anthropogenic emissions exhibit a more spatially dispersed  
387 distribution across the continent (Fig. S3d), resulting in the highest demand for additional observation sites.  
388 To satisfy the same marginal gain criterion, 21 new sites are required in both January and July. Notably, this  
389 value corresponds to the upper limit of the candidate pool, and the marginal gain criterion is not fully satisfied  
390 in the January case, suggesting that the true optimal network size for anthropogenic emissions likely exceeds  
391 the currently available candidate locations.

392 As an aggregate of sectoral contributions, the optimal number of additional sites for total CH<sub>4</sub> emissions falls  
393 between those of the source sectors, yielding optimal values of 7 in January and 10 in July. For the subsequent  
394 configuration optimization, we adopt the July-derived optimal site number (10 sites) as the target network  
395 size. This choice is motivated by the fact that July represents a season with systematically higher CH<sub>4</sub>  
396 emissions across most sectors except for anthropogenic sources (Fig. S4), implying stronger atmospheric  
397 signals and enhanced spatial overlap among source influences. Designing the network under this more  
398 emission-intensive scenario provides a stringent and practically relevant benchmark, ensuring that the  
399 selected configuration remains effective during periods of elevated emissions.



400

401 **Figure 4. Mean uncertainty reduction  $P(n)$  as a function of added station number for (a) total, (b) fire,**  
 402 **(c) wetland, and (d) anthropogenic  $\text{CH}_4$  emissions, and for January (blue lines) and July (red lines)**  
 403 **separately.** The deep-colored lines denote the ensemble mean uncertainty reductions ( $P(n)$  on the left axis),  
 404 while light-colored lines denote the relative marginal gain  $\Delta P(n)$  on the right axis. The ten-site with star  
 405 marker in (a) is selected as the optimal new site number.

### 406 3.3 Optimal site configurations with the optimal number

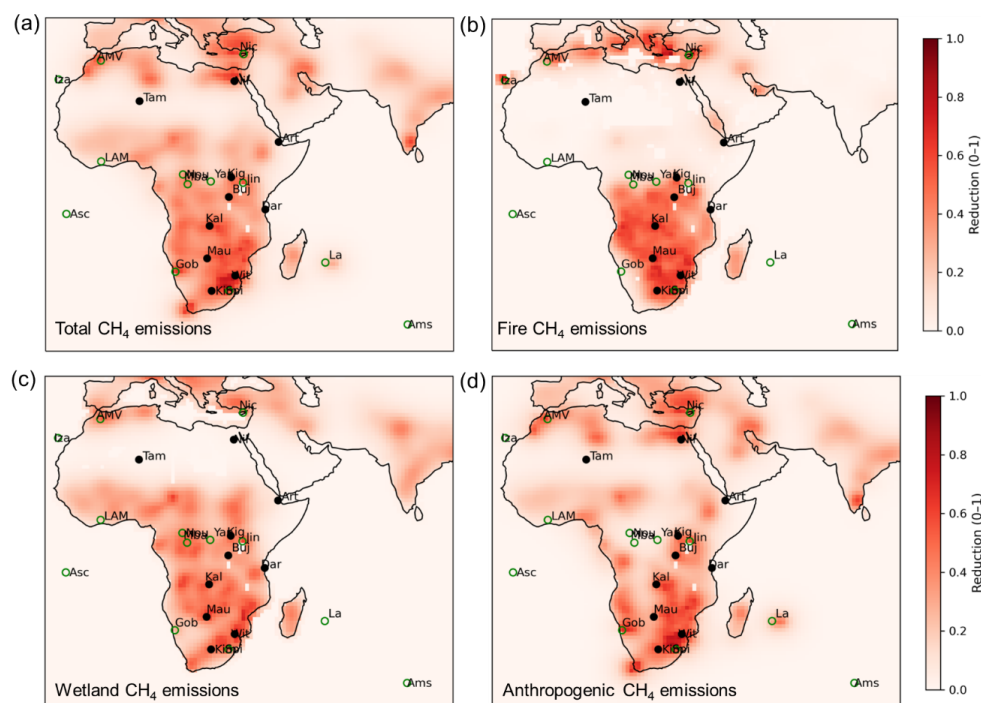
407 We next examine the spatial configuration of observation sites under the optimized network size and assess  
 408 its effectiveness in constraining total and sectoral  $\text{CH}_4$  emissions. Figure 5 shows the spatial distribution of  
 409 uncertainty reduction for total, fire, wetland, and anthropogenic  $\text{CH}_4$  emissions in July, obtained using the  
 410 optimal 10-site configuration (January results are shown in Fig. S9). The optimized configuration is selected  
 411 as the best-performing solution among all candidate site combinations in the ensemble, ensuring  
 412 comprehensive and robust exploration of the configuration space (Fig. S10).

413 The ten sites contributing most strongly to the total uncertainty reduction are Nile, Tamanrasset, Arta, Kigali,  
 414 Bujumbura, DaresSalam, Kalene, Maun, Wits, and Kimberley (closed black circles in Figs. 5 and S9). This  
 415 configuration reduces the posterior uncertainty of total African  $\text{CH}_4$  emissions by 69% in January and 73%  
 416 in July. These values are close to the 71% and 73% reductions achieved in January and July, respectively,  
 417 under the idealized scenario in which all 34 sites are deployed (Section 3.1). This comparison demonstrates  
 418 that the majority of the attainable information gain can be captured by a carefully optimized subset of sites,  
 419 without resorting to a uniformly dense and substantially more costly network. At the sectoral level, the  
 420 optimized configuration achieves uncertainty reductions of 91% and 94% for fire emissions, 87% and 84%



421 for wetland emissions, and 68% and 65% for anthropogenic emissions in January and July, respectively.  
422 Overall, more than 65% uncertainty reduction is attained across all sectors with only ten additional stations,  
423 highlighting the efficiency of the optimized network design.

424 The spatial arrangement of the selected sites reveals a deliberately dispersed and complementary network  
425 across the African continent, designed to balance source-region coverage and inter-site spacing while  
426 minimizing redundant transport sensitivities. In northern Africa, the inclusion of site Nile and Tamanrasset  
427 substantially enhance sensitivity to anthropogenic CH<sub>4</sub> emissions associated with irrigated croplands and  
428 densely populated regions, which are weakly constrained by the existing observing network. Across  
429 equatorial Africa, sites such as Arta, Kigali, Bujumbura, DaresSalam, and Kalene are distributed along a  
430 north–south corridor spanning the Congo Basin and its surroundings. This alignment closely follows the core  
431 wetland CH<sub>4</sub> emission hotspots while maintaining sufficient separation from existing and planned stations,  
432 thereby reducing footprint overlap and maximizing the marginal information gain of each site. In southern  
433 Africa, the combination of Maun, Wits, and Kimberley strengthens constraints across multiple sectors  
434 simultaneously, improving sensitivity to wetland emissions in the Okavango region as well as to fire and  
435 anthropogenic emissions over southern Africa. Although the optimized sites are all located within Africa,  
436 their impact on uncertainty reduction is not confined to the continent. Owing to large-scale atmospheric  
437 transport, secondary uncertainty reductions extend into adjacent regions such as the Middle East and parts of  
438 South Asia (Fig. 5), providing an additional benefit of the optimized African observing network beyond its  
439 primary target region.



440



441 **Figure 5. Spatial distribution of uncertainty reduction for (a) total; (b) fire; (c) wetland; and (d)**  
442 **anthropogenic CH<sub>4</sub> emissions with the 10 optimal site configurations in 2025 July.** The 10 optimal sites  
443 in this case include Nile, Tamanrasset, Arta, Kigali, Bujumbura, DaresSalam, Kalene, Maun, Wits, and  
444 Kimberley. All the site names are abbreviated with their first three letters. The green open circles are 9  
445 operational and 4 planned sites, and the closed black circles are optimized new 10 sites. The map for January  
446 is provided in Fig. S9.

#### 447 **3.4 Evaluation of the network design framework**

448 We evaluate the robustness and practical applicability of the optimized network using three complementary  
449 analyses based on the July total CH<sub>4</sub> emission case, which represents the most emission-intensive season (Fig.  
450 S4): sensitivity tests to key assumptions, ranking of candidate sites under the default setting, and a randomly  
451 perturbed-prior experiment (Fig. 6).

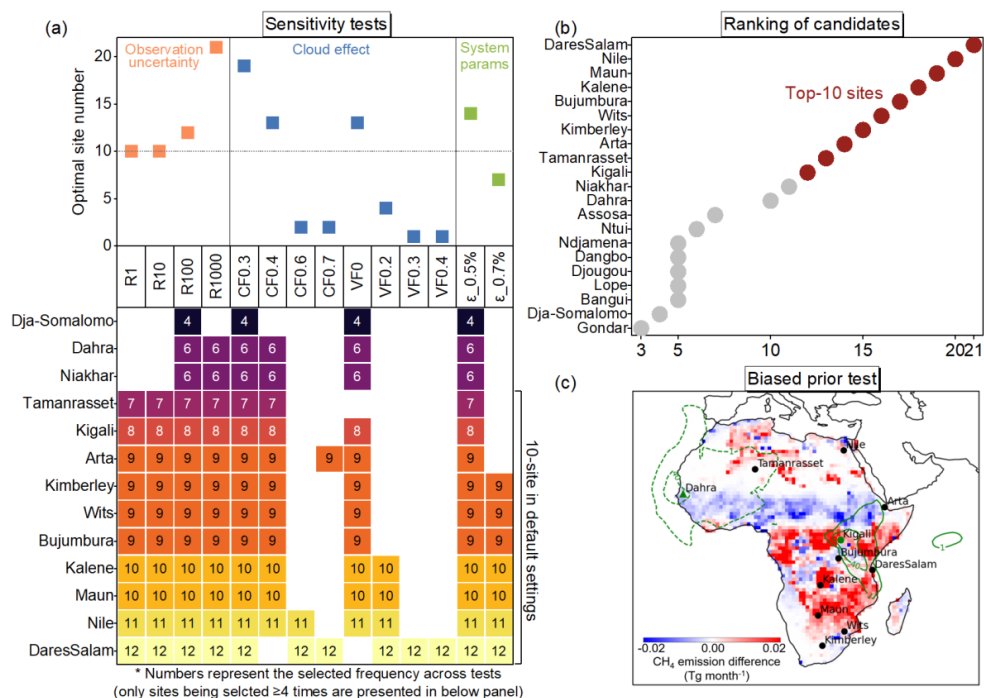
452 Sensitivity experiments explore variations in observational uncertainty, cloud-related constraints, and major  
453 system parameter (Table S4), examining both the optimal number of additional sites and the corresponding  
454 best configurations (Fig. 6a). Across the 14 tests, the optimal site number shows clear dependence on  
455 assumptions that control effective observational coverage. In particular, cloud-related parameters exert the  
456 strongest influence. Stricter cloud screening, implemented through lower cloud fraction thresholds (i.e., less  
457 data available during cloudy periods) or more restrictive minimum valid fraction (i.e., a higher required  
458 fraction of cloud-free days) requirements, reduces data availability and increases the number of sites required  
459 to satisfy the marginal gain criterion ( $\epsilon$ ). The optimal number of additional sites increases to 13 when the  
460 minimum valid fraction is set to zero (VF0) and up to 19 when the cloud fraction threshold is reduced below  
461 0.3. In contrast, the spatial configuration of selected sites remains highly consistent. The default ten-site  
462 solution (Nile, Tamanrasset, Arta, Kigali, Bujumbura, DaresSalam, Kalene, Maun, Wits, and Kimberley) is  
463 repeatedly recovered across tests, indicating that once network size is prescribed, the optimization converges  
464 toward a stable core set of locations that provide complementary and nonredundant information.

465 Beyond identifying a single optimal configuration, the framework also provides a quantitative prioritization  
466 of candidate sites. Under the default parameter setting, optimization is repeated for prescribed network sizes  
467 ranging from 1 to 21 additional sites, and the selection frequency of each site is recorded (Fig. 6b). Sites  
468 selected more frequently can be interpreted as having higher priority in sequential network expansion.  
469 Notably, the top ten ranked sites correspond exactly to the ten-site optimal configuration, demonstrating  
470 internal consistency of the framework. This ranking capability offers a practical alternative use of the system:  
471 given a predefined number of stations constrained by budget or logistics, the framework can directly provide  
472 a prioritized deployment strategy.

473 To assess dependence on the assumed prior emission distribution, we further conduct a randomly perturbed-  
474 prior experiment in which July CH<sub>4</sub> emissions are spatially shifted and rescaled, generating modified hotspot  
475 patterns (Figs. 6c and S11). The optimized configuration derived under the perturbed prior retains the overall  
476 spatial structure of the base solution but exhibits targeted adjustments. Specifically, Kigali is replaced by  
477 Dahra, reflecting enhanced sensitivity to regions where emissions increase under the perturbed prior without



478 sufficient observational constraint. The associated transport footprints confirm that these newly selected sites  
 479 better capture the redistributed emission signals. This adaptive response indicates that the optimization is not  
 480 rigidly tied to a fixed prior assumption; rather, site placement dynamically adjusts to changes in emission  
 481 patterns while preserving the physically constrained backbone of the network.



482

483 **Figure 6. Evaluation of site optimization framework.** (a) Sensitivity tests. The upper panel shows the  
 484 optimal number of additional sites under different parameter settings and the lower panel shows the  
 485 corresponding optimal configurations. See Tables S3–S4 for full test descriptions. R denotes observation  
 486 uncertainty; CF cloud fraction threshold; VF minimum valid fraction; and the marginal gain threshold  $\epsilon$ . (b)  
 487 Ranking of candidate sites under the default setting, which shows how frequently each site is selected across  
 488 network sizes from 1 to 21 additional sites. (c) Biased-prior test. Shading shows July CH<sub>4</sub> total prior  
 489 differences (perturbed-base). Black markers denote sites selected under both priors; green circles sites unique  
 490 to the base prior (Kigali); green triangles sites unique to the perturbed prior (Dahra). Green contours show 3-  
 491 day footprints for sites unique to each case (solid: base; dashed: perturbed). Sectoral difference of  
 492 perturbation is seen in Fig. S11.

#### 493 4. Discussion

494 This study provides a quantitative and transferable framework for designing XCH<sub>4</sub> observation networks in  
 495 data-sparse regions, with Africa serving as a representative and policy-relevant case. By explicitly accounting  
 496 for diminishing returns in uncertainty reduction, transport sensitivity overlap, and cloud-related observational  
 497 limitations, the proposed strategic Bayesian framework demonstrates that substantial improvements in  
 498 emission constraints can be achieved without a uniformly dense network expansion. Importantly, the



499 framework is implemented within a global inversion system, with transport sensitivities derived from adjoint  
500 simulations of the LMDZ model at ~90 km resolution and prior error covariance defined over the entire globe.  
501 This global configuration avoids the need for lateral boundary conditions required by regional models and  
502 ensures that optimized site configurations are evaluated consistently within large-scale atmospheric transport  
503 pathways. Applied to Africa, the results show that uncertainty reduction rapidly improves with the first few  
504 additional sites but saturates thereafter, highlighting a strong nonlinearity between network size and  
505 information gain. For total African CH<sub>4</sub> emissions, an optimized configuration of ten additional sites captures  
506 more than 65% of the achievable uncertainty reduction in both January and July, approaching the  
507 performance of an idealized scenario in which all candidate sites are deployed. Sectoral diagnostics further  
508 show that network-size requirements depend on the spatial heterogeneity and seasonal redistribution of  
509 dominant source regions, underscoring the importance of targeted rather than uniform deployment.

510 The reported uncertainty reductions represent potential information gain within a Bayesian covariance  
511 framework rather than direct predictions of operational inversion performance. Several simplifying  
512 assumptions are adopted, including the omission of sub-monthly and subpixel emission variability, use of  
513 half-month adjoint sensitivities, prescribed and spatially uniform observation uncertainties, and omission of  
514 aerosol impacts on retrieval sensitivity. Uncertainty reduction is evaluated under assumed prior covariance  
515 structures and does not explicitly account for source mixing, sector attribution errors, representation errors,  
516 or structural model biases, which are inherent to most Bayesian inversion systems. These idealized  
517 assumptions likely contribute to the relatively high theoretical reductions. For example, neglecting aerosol  
518 impacts may overestimate effective data availability and thereby inflate the inferred uncertainty reduction  
519 (Schooling et al., 2026). Consequently, the reported reductions serve primarily as relative metrics for network  
520 comparison and prioritization rather than absolute estimates of achievable inversion accuracy. Nonetheless,  
521 sensitivity experiments indicate that although the optimal network size responds to assumptions affecting  
522 observational effectiveness, particularly cloud screening, the spatial configuration of selected sites remains  
523 highly robust. This stability suggests that site selection is fundamentally constrained by the large-scale  
524 structure of CH<sub>4</sub> emissions and atmospheric transport pathways.

525 Despite these limitations, the framework offers a powerful and flexible tool for guiding observation  
526 deployment decisions. Because uncertainty reduction is evaluated at the grid scale and can be spatially  
527 aggregated, the results can be readily translated into country- or region-level metrics, enabling the  
528 identification and ranking of areas that benefit most from optimized network expansion. In the African case,  
529 several major methane emitting countries, including South Africa, the Democratic Republic of the Congo,  
530 Angola, and Algeria, consistently achieve uncertainty reductions exceeding 50% in both January and July  
531 under the proposed ten-site optimal configuration (Fig. S12 and Table S5). This demonstrates that a relatively  
532 small, strategically designed network can substantially improve emission constraints across national and  
533 regional scales. More broadly, the framework can, in principle, be adapted to other greenhouse gases, regions,  
534 and observing systems, including hybrid networks that combine ground-based and satellite measurements.  
535 Such extensions would require gas-specific prior uncertainty structures, transport sensitivities, and



536 observational characteristics, and would likely lead to different optimization criteria and network  
537 configurations. In this sense, the present study contributes a transferable and systematically implemented  
538 framework for evidence-based observation network design, supporting both scientific applications and  
539 policy-relevant assessments of greenhouse gas emissions in data-sparse regions.

540

541 *Code and data availability.* The version of the LMDZ-INCA model used in this study is available from:  
542 <https://forge.ipsl.jussieu.fr/igcmg/svn/modipls/trunk>. All the meteorological factors (cloud cover, 10-m wind  
543 fields, and convective available potential energy) are acquired from ERA5 dataset at  
544 <https://cds.climate.copernicus.eu/datasets/reanalysis-era5-land-monthly-means?tab=overview>. The sources  
545 of prior datasets adopted are detailed in Table S1. The codes and scripts developed for estimation, plotting,  
546 and other analysis are accessible upon reasonable request from the corresponding author.

547 *Supplement.* The supplement related to this article is available online.

548 *Author Contributions.* HL and PC designed this study. HL conducted the system establishment, analyzed the  
549 data, and wrote the draft. PC, BZ, PP, and BP supervised the study, helped data analysis, reviewed and edited  
550 the paper. FC performed the footprint simulations, helped data analysis, and edited the paper. SP offered the  
551 prior file, reviewed and edited the paper. FH, ML, EO, DM, MR, JC, and LS reviewed and edited the paper.  
552 All the co-authors contributed to the revision of this paper.

553 *Competing interests.* The authors declare that they have no conflict of interest.

554 *Acknowledgements.* The authors thank the editor and the anonymous referees for helpful comments that have  
555 improved the paper.

556 *Financial support.* This work was granted access to the HPC resources of CCRT under the allocation  
557 CEA/DRF, and of TGCC under the allocation A0190102201 made by GENCI.

558



## 559 References

- 560 Adame, J. A., Padilla, R., Gutierrez-Alvarez, I., Bogeat, J. A., Lopez, A., and Yela, M.: Greenhouse gases in  
561 the tall tower of El Arenosillo station in Southwestern Europe: First-year of measurements, *Atmospheric*  
562 *Research*, 299, 107221, <https://doi.org/10.1016/j.atmosres.2024.107221>, 2024.
- 563 Alberti, C., Hase, F., Frey, M., Dubravica, D., Blumenstock, T., Dehn, A., Castracane, P., Surawicz, G.,  
564 Harig, R., Baier, B. C., Bès, C., Bi, J., Boesch, H., Butz, A., Cai, Z., Chen, J., Crowell, S. M., Deutscher, N.  
565 M., Ene, D., Franklin, J. E., Garcia, O., Griffith, D., Grouiez, B., Grutter, M., Hamdouni, A., Houweling, S.,  
566 Humpage, N., Jacobs, N., Jeong, S., Joly, L., Jones, N. B., Jouglet, D., Kivi, R., Kleinschek, R., Lopez, M.,  
567 Medeiros, D. J., Morino, I., Mostafavipak, N., Müller, A., Ohyama, H., Palmer, P. I., Pathakoti, M., Pollard,  
568 D. F., Raffalski, U., Ramonet, M., Ramsay, R., Sha, M. K., Shiomi, K., Simpson, W., Stremme, W., Sun, Y.,  
569 Tanimoto, H., Té, Y., Tsidu, G. M., Velazco, V. A., Vogel, F., Watanabe, M., Wei, C., Wunch, D., Yamasoe,  
570 M., Zhang, L., and Orphal, J.: Improved calibration procedures for the EM27/SUN spectrometers of the  
571 Collaborative Carbon Column Observing Network (COCCON), *Atmos. Meas. Tech.*, 15, 2433-2463,  
572 10.5194/amt-15-2433-2022, 2022.
- 573 Barthel, M., Bauters, M., Baumgartner, S., Drake, T. W., Bey, N. M., Bush, G., Boeckx, P., Botefa, C. I.,  
574 Dériaz, N., Ekamba, G. L., Gallarotti, N., Mbayu, F. M., Mugula, J. K., Makelele, I. A., Mbongo, C. E.,  
575 Mohn, J., Manda, J. Z., Mpambi, D. M., Ntaboba, L. C., Rukeza, M. B., Spencer, R. G. M., Summerauer,  
576 L., Vanlauwe, B., Van Oost, K., Wolf, B., and Six, J.: Low N<sub>2</sub>O and variable CH<sub>4</sub> fluxes from tropical forest  
577 soils of the Congo Basin, *Nature Communications*, 13, 330, 10.1038/s41467-022-27978-6, 2022.
- 578 Chevallier, F., Martinez, A., Lloret, Z., Takache, S., and Cozic, A.: Offline Atmospheric Transport on a  
579 Global Mesh of Hexagons, *Journal of Geophysical Research: Atmospheres*, 130, e2025JD043579,  
580 <https://doi.org/10.1029/2025JD043579>, 2025.
- 581 Choudhury, G. and Goren, T.: Sampling Bias From Satellite Retrieval Failures of Cloud Properties and Its  
582 Implications for Aerosol-Cloud Interactions, *Geophysical Research Letters*, 52, e2025GL115429,  
583 <https://doi.org/10.1029/2025GL115429>, 2025.
- 584 Ciais, P., Bombelli, A., Williams, M., Piao, S. L., Chave, J., Ryan, C. M., Henry, M., Brender, P., and  
585 Valentini, R.: The carbon balance of Africa: synthesis of recent research studies, *Philosophical Transactions*  
586 *of the Royal Society A: Mathematical, Physical and Engineering Sciences*, 369, 2038-2057,  
587 10.1098/rsta.2010.0328, 2011.
- 588 Cressot, C., Pison, I., Rayner, P. J., Bousquet, P., Fortems-Cheiney, A., and Chevallier, F.: Can we detect  
589 regional methane anomalies? A comparison between three observing systems, *Atmos. Chem. Phys.*, 16,  
590 9089-9108, 10.5194/acp-16-9089-2016, 2016.
- 591 Cressot, C., Chevallier, F., Bousquet, P., Crevoisier, C., Dlugokencky, E. J., Fortems-Cheiney, A.,  
592 Frankenberg, C., Parker, R., Pison, I., Scheepmaker, R. A., Montzka, S. A., Krummel, P. B., Steele, L. P.,  
593 and Langenfelds, R. L.: On the consistency between global and regional methane emissions inferred from  
594 SCIAMACHY, TANSO-FTS, IASI and surface measurements, *Atmos. Chem. Phys.*, 14, 577-592,  
595 10.5194/acp-14-577-2014, 2014.
- 596 Crippa, M., Guizzardi, D., Pagani, F., Schiavina, M., Melchiorri, M., Pisoni, E., Graziosi, F., Muntean, M.,  
597 Maes, J., Dijkstra, L., Van Damme, M., Clarisse, L., and Coheur, P.: Insights into the spatial distribution of  
598 global, national, and subnational greenhouse gas emissions in the Emissions Database for Global  
599 Atmospheric Research (EDGAR v8.0), *Earth Syst. Sci. Data*, 16, 2811-2830, 10.5194/essd-16-2811-2024,  
600 2024.
- 601 Doc, J., Bréon, F. M., Lopez, M., Té, Y., Jeseck, P., Lian, J., Nief, G., Parent, A., Leuridan, H., and Ramonet,  
602 M.: Two years of total column measurements of CO<sub>2</sub>, CH<sub>4</sub> and CO in Paris, France, *EGUsphere*, 2025, 1-32,  
603 10.5194/egusphere-2025-4876, 2025.
- 604 Eames, T., Schutgens, N., Ioannidis, E., van der Velde, I. R., van Gerrevink, M. J., Vernooij, R., and van der  
605 Werf, G. R.: Radiative forcing due to shifting southern African fire regimes, *Atmos. Chem. Phys.*, 25, 17429-  
606 17453, 10.5194/acp-25-17429-2025, 2025.
- 607 Ernst, Y., Archibald, S., Balzter, H., Chevallier, F., Ciais, P., Fischer, C. G., Gaubert, B., Higginbottom, T.,  
608 Higgins, S., Lawal, S., Lacroix, F., Lauerwald, R., Lourenco, M., Martens, C., Mengistu, A. G., Merbold, L.,  
609 Mitchard, E., Moyo, M., Nguyen, H., O'Sullivan, M., Rodriguez-Veiga, P., Rosan, T., Rosentreter, J., Ryan,  
610 C., Scheiter, S., Sitch, S., Stevens, N., Tagesson, T., Tian, H., Wang, M., Woon, J. S., Zheng, B., Zhou, Y.,  
611 and Scholes, R. J.: The African Regional Greenhouse Gases Budget (2010–2019), *Global Biogeochemical*  
612 *Cycles*, 38, e2023GB008016, <https://doi.org/10.1029/2023GB008016>, 2024.



- 613 Feng, L., Palmer, P. I., Parker, R. J., Lunt, M. F., and Bösch, H.: Methane emissions are predominantly  
614 responsible for record-breaking atmospheric methane growth rates in 2020 and 2021, *Atmos. Chem. Phys.*,  
615 23, 4863-4880, 10.5194/acp-23-4863-2023, 2023.
- 616 Frey, M., Sha, M. K., Hase, F., Kiel, M., Blumenstock, T., Harig, R., Surawicz, G., Deutscher, N. M., Shiomi,  
617 K., Franklin, J. E., Bösch, H., Chen, J., Grutter, M., Ohyama, H., Sun, Y., Butz, A., Mengistu Tsidu, G., Ene,  
618 D., Wunch, D., Cao, Z., Garcia, O., Ramonet, M., Vogel, F., and Orphal, J.: Building the Collaborative  
619 Carbon Column Observing Network (COCCON): long-term stability and ensemble performance of the  
620 EM27/SUN Fourier transform spectrometer, *Atmos. Meas. Tech.*, 12, 1513-1530, 10.5194/amt-12-1513-  
621 2019, 2019.
- 622 Ganesan, A. L., Manning, A. J., Grant, A., Young, D., Oram, D. E., Sturges, W. T., Moncrieff, J. B., and  
623 O'Doherty, S.: Quantifying methane and nitrous oxide emissions from the UK and Ireland using a national-  
624 scale monitoring network, *Atmos. Chem. Phys.*, 15, 6393-6406, 10.5194/acp-15-6393-2015, 2015.
- 625 Gaubert, B., Stephens, B. B., Baker, D. F., Basu, S., Bertolacci, M., Bowman, K. W., Buchholz, R., Chatterjee,  
626 A., Chevallier, F., Commane, R., Cressie, N., Deng, F., Jacobs, N., Johnson, M. S., Maksyutov, S. S., McKain,  
627 K., Liu, J., Liu, Z., Morgan, E., O'Dell, C., Philip, S., Ray, E., Schimel, D., Schuh, A., Taylor, T. E., Weir,  
628 B., van Wees, D., Wofsy, S. C., Zammit-Mangion, A., and Zeng, N.: Neutral Tropical African CO<sub>2</sub> Exchange  
629 Estimated From Aircraft and Satellite Observations, *Global Biogeochemical Cycles*, 37, e2023GB007804,  
630 <https://doi.org/10.1029/2023GB007804>, 2023.
- 631 Gunaratne, T., Liyanage, S., Punchihewa, C., Badurdeen, S., and Jayathilaka, R.: Unmasking climate  
632 vulnerability in Africa: the role of CO<sub>2</sub> and CH<sub>4</sub> emissions on rising temperatures and sea levels, *Humanities*  
633 and *Social Sciences Communications*, 12, 601, 10.1057/s41599-025-04890-0, 2025.
- 634 Hase, F., Frey, M., Kiel, M., Blumenstock, T., Harig, R., Keens, A., and Orphal, J.: Addition of a channel for  
635 XCO observations to a portable FTIR spectrometer for greenhouse gas measurements, *Atmos. Meas. Tech.*,  
636 9, 2303-2313, 10.5194/amt-9-2303-2016, 2016.
- 637 Helfter, C., Gondwe, M., Murray-Hudson, M., Makati, A., and Skiba, U.: From sink to source: high inter-  
638 annual variability in the carbon budget of a Southern African wetland, *Philosophical Transactions of the*  
639 *Royal Society A: Mathematical, Physical and Engineering Sciences*, 380, 10.1098/rsta.2021.0148, 2021.
- 640 Hersbach, H., Bell, B., Berrisford, P., Hirahara, S., Horányi, A., Muñoz-Sabater, J., Nicolas, J., Peubey, C.,  
641 Radu, R., Schepers, D., Simmons, A., Soci, C., Abdalla, S., Abellan, X., Balsamo, G., Bechtold, P., Biavati,  
642 G., Bidlot, J., Bonavita, M., De Chiara, G., Dahlgren, P., Dee, D., Diamantakis, M., Dragani, R., Flemming,  
643 J., Forbes, R., Fuentes, M., Geer, A., Haimberger, L., Healy, S., Hogan, R. J., Hólm, E., Janisková, M.,  
644 Keeley, S., Laloyaux, P., Lopez, P., Lupu, C., Radnoti, G., de Rosnay, P., Rozum, I., Vamborg, F., Villaume,  
645 S., and Thépaut, J.-N.: The ERA5 global reanalysis, *Quarterly Journal of the Royal Meteorological Society*,  
646 146, 1999-2049, 10.1002/qj.3803, 2020.
- 647 Hourdin, F., Rio, C., Grandpeix, J.-Y., Madeleine, J.-B., Cheruy, F., Rochetin, N., Jam, A., Musat, I., Idelkadi,  
648 A., Fairhead, L., Foujols, M.-A., Mellul, L., Traore, A.-K., Dufresne, J.-L., Boucher, O., Lefebvre, M.-P.,  
649 Millour, E., Vignon, E., Jouhaud, J., Diallo, F. B., Lott, F., Gastineau, G., Caubel, A., Meurdesoif, Y., and  
650 Ghattas, J.: LMDZ6A: The Atmospheric Component of the IPSL Climate Model With Improved and Better  
651 Tuned Physics, *Journal of Advances in Modeling Earth Systems*, 12, e2019MS001892,  
652 <https://doi.org/10.1029/2019MS001892>, 2020.
- 653 Humpage, N., Boesch, H., Okello, W., Chen, J., Dietrich, F., Lunt, M. F., Feng, L., Palmer, P. I., and Hase,  
654 F.: Greenhouse gas column observations from a portable spectrometer in Uganda, *Atmos. Meas. Tech.*, 17,  
655 5679-5707, 10.5194/amt-17-5679-2024, 2024.
- 656 Kadyrov, N., Broquet, G., Chevallier, F., Rivier, L., Gerbig, C., and Ciais, P.: On the potential of the ICOS  
657 atmospheric CO<sub>2</sub> measurement network for estimating the biogenic CO<sub>2</sub> budget of Europe, *Atmos. Chem.*  
658 *Phys.*, 15, 12765-12787, 10.5194/acp-15-12765-2015, 2015.
- 659 Kaiser, J. W., Heil, A., Andreae, M. O., Benedetti, A., Chubarova, N., Jones, L., Morcrette, J. J., Razinger,  
660 M., Schultz, M. G., Suttie, M., and van der Werf, G. R.: Biomass burning emissions estimated with a global  
661 fire assimilation system based on observed fire radiative power, *Biogeosciences*, 9, 527-554, 10.5194/bg-9-  
662 527-2012, 2012.
- 663 Kaminski, T. and Rayner, P. J.: Reviews and syntheses: guiding the evolution of the observing system for  
664 the carbon cycle through quantitative network design, *Biogeosciences*, 14, 4755-4766, 10.5194/bg-14-4755-  
665 2017, 2017.
- 666 Keppel-Aleks, G., Randerson, J. T., Lindsay, K., Stephens, B. B., Keith Moore, J., Doney, S. C., Thornton,  
667 P. E., Mahowald, N. M., Hoffman, F. M., Sweeney, C., Tans, P. P., Wennberg, P. O., and Wofsy, S. C.:  
668 Atmospheric Carbon Dioxide Variability in the Community Earth System Model: Evaluation and Transient



- 669 Dynamics during the Twentieth and Twenty-First Centuries, *Journal of Climate*, 26, 4447-4475,  
670 <https://doi.org/10.1175/JCLI-D-12-00589.1>, 2013.
- 671 Kurganskiy, A., Feng, L., Humpage, N., Palmer, P. I., Woodwark, A. J. P., Doniki, S., and Weidmann, D.:  
672 The Greenhouse gas Emission Monitoring network to Inform Net-zero Initiatives UK (GEMINI-UK):  
673 network design, theoretical performance, and initial data, *Atmos. Meas. Tech.*, 18, 7525-7563, 10.5194/amt-  
674 18-7525-2025, 2025.
- 675 Lauvaux, T., Schuh, A. E., Bocquet, M., Wu, L., Richardson, S., Miles, N., and Davis, K. J.: Network design  
676 for mesoscale inversions of CO<sub>2</sub> sources and sinks, *Tellus B: Chemical and Physical Meteorology*, 64, 17980,  
677 10.3402/tellusb.v64i0.17980, 2012.
- 678 Liu, S., Wei, K., Chen, B., Jin, Z., Chen, Z., Wu, Z., Fan, Z., Li, S., Zang, K., Zhang, C., Xu, H., De Maeyer,  
679 P., and Fang, S.: Unveiling High-Resolution CH<sub>4</sub> Profiles Over Southeast China: Novel Insights From  
680 AirCore Balloon Observations, *Geophysical Research Letters*, 52, e2025GL116203,  
681 <https://doi.org/10.1029/2025GL116203>, 2025.
- 682 Lunt, M. F., Palmer, P. I., Feng, L., Taylor, C. M., Boesch, H., and Parker, R. J.: An increase in methane  
683 emissions from tropical Africa between 2010 and 2016 inferred from satellite data, *Atmos. Chem. Phys.*, 19,  
684 14721-14740, 10.5194/acp-19-14721-2019, 2019.
- 685 McDuffie, E. E., Smith, S. J., O'Rourke, P., Tibrewal, K., Venkataraman, C., Marais, E. A., Zheng, B., Crippa,  
686 M., Brauer, M., and Martin, R. V.: A global anthropogenic emission inventory of atmospheric pollutants  
687 from sector- and fuel-specific sources (1970–2017): an application of the Community Emissions Data System  
688 (CEDS), *Earth Syst. Sci. Data*, 12, 3413-3442, 10.5194/essd-12-3413-2020, 2020.
- 689 Mengistu, A. G. and Mengistu Tsidu, G.: On the performance of satellite-based observations of XCO<sub>2</sub> in  
690 capturing the NOAA Carbon Tracker model and ground-based flask observations over Africa's land mass,  
691 *Atmos. Meas. Tech.*, 13, 4009-4033, 10.5194/amt-13-4009-2020, 2020.
- 692 Merbold, L., Scholes, R. J., Acosta, M., Beck, J., Bombelli, A., Fiedler, B., Grieco, E., Helmschrot, J., Hugo,  
693 W., Kasurinen, V., Kim, D.-G., Körtzinger, A., Leitner, S., López-Ballesteros, A., Ndisi, M., Nickless, A.,  
694 Salmon, E., Saunders, M., Skjelvan, I., Vermeulen, A. T., and Kutsch, W. L.: Opportunities for an African  
695 greenhouse gas observation system, *Regional Environmental Change*, 21, 104, 10.1007/s10113-021-01823-  
696 w, 2021.
- 697 Mostefaoui, M., Ciais, P., McGrath, M. J., Peylin, P., Patra, P. K., and Ernst, Y.: Greenhouse gas emissions  
698 and their trends over the last 3 decades across Africa, *Earth Syst. Sci. Data*, 16, 245-275, 10.5194/essd-16-  
699 245-2024, 2024.
- 700 Nickless, A., Scholes, R. J., Vermeulen, A., Beck, J., López-Ballesteros, A., Ardö, J., Karstens, U., Rigby,  
701 M., Kasurinen, V., Pantazatou, K., Jorch, V., and Kutsch, W.: Greenhouse gas observation network design  
702 for Africa, *Tellus B: Chemical and Physical Meteorology*, 10.1080/16000889.2020.1824486, 2020a.
- 703 Nickless, A., Scholes, R. J., Vermeulen, A., Beck, J., López-Ballesteros, A., Ardö, J., Karstens, U., Rigby,  
704 M., Kasurinen, V., Pantazatou, K., Jorch, V., and Kutsch, W.: Greenhouse gas observation network design  
705 for Africa, *Tellus B: Chemical and Physical Meteorology*, 72, 1-30, 10.1080/16000889.2020.1824486, 2020b.
- 706 Palmer, P. I., Wilson, E. L., L. Villanueva, G., Liuzzi, G., Feng, L., DiGregorio, A. J., Mao, J., Ott, L., and  
707 Duncan, B.: Potential improvements in global carbon flux estimates from a network of laser heterodyne  
708 radiometer measurements of column carbon dioxide, *Atmos. Meas. Tech.*, 12, 2579-2594, 10.5194/amt-12-  
709 2579-2019, 2019.
- 710 Park, H., Jeong, S., Sha, M. K., Lee, J., and Frey, M. M.: Comparisons of Greenhouse Gas Observation  
711 Satellite Performances Over Seoul Using a Portable Ground-Based Spectrometer, *Geophysical Research  
712 Letters*, 51, e2024GL109334, <https://doi.org/10.1029/2024GL109334>, 2024.
- 713 Pollard, D. F., Robinson, J., Shiona, H., and Smale, D.: Intercomparison of Total Carbon Column Observing  
714 Network (TCCON) data from two Fourier transform spectrometers at Lauder, New Zealand, *Atmos. Meas.  
715 Tech.*, 14, 1501-1510, 10.5194/amt-14-1501-2021, 2021.
- 716 Qu, Z., Jacob, D. J., Zhang, Y., Shen, L., Varon, D. J., Lu, X., Scarpelli, T., Bloom, A., Worden, J., and  
717 Parker, R. J.: Attribution of the 2020 surge in atmospheric methane by inverse analysis of GOSAT  
718 observations, *Environmental Research Letters*, 17, 094003, 10.1088/1748-9326/ac8754, 2022.
- 719 Rayner, P. J., Michalak, A. M., and Chevallier, F.: Fundamentals of data assimilation applied to  
720 biogeochemistry, *Atmos. Chem. Phys.*, 19, 13911-13932, 10.5194/acp-19-13911-2019, 2019.
- 721 Rodgers, C. D.: Inverse Methods for Atmospheric Sounding, *Inverse Methods for Atmospheric Sounding*,  
722 10.1142/3171, 2000.
- 723 SASAKAWA, M., SHIMOYAMA, K., MACHIDA, T., TSUDA, N., SUTO, H., ARSHINOV, M.,  
724 DAVYDOV, D., FOFONOV, A., KRASNOV, O., SAEKI, T., KOYAMA, Y., and MAKSYUTOV, S.:



725 Continuous measurements of methane from a tower network over Siberia, *Tellus B*, 62, 403-416,  
726 <https://doi.org/10.1111/j.1600-0889.2010.00494.x>, 2010.  
727 Saunois, M., Martinez, A., Poulter, B., Zhang, Z., Raymond, P. A., Regnier, P., Canadell, J. G., Jackson, R.  
728 B., Patra, P. K., Bousquet, P., Ciais, P., Dlugokencky, E. J., Lan, X., Allen, G. H., Bastviken, D., Beerling,  
729 D. J., Belikov, D. A., Blake, D. R., Castaldi, S., Crippa, M., Deemer, B. R., Dennison, F., Etiope, G., Gedney,  
730 N., Höglund-Isaksson, L., Holgerson, M. A., Hopcroft, P. O., Hugelius, G., Ito, A., Jain, A. K., Janardanan,  
731 R., Johnson, M. S., Kleinen, T., Krummel, P. B., Lauerwald, R., Li, T., Liu, X., McDonald, K. C., Melton, J.  
732 R., Mühle, J., Müller, J., Murguia-Flores, F., Niwa, Y., Noce, S., Pan, S., Parker, R. J., Peng, C., Ramonet,  
733 M., Riley, W. J., Rocher-Ros, G., Rosentretter, J. A., Sasakawa, M., Segers, A., Smith, S. J., Stanley, E. H.,  
734 Thanwerdas, J., Tian, H., Tsuruta, A., Tubiello, F. N., Weber, T. S., van der Werf, G. R., Worthy, D. E. J.,  
735 Xi, Y., Yoshida, Y., Zhang, W., Zheng, B., Zhu, Q., Zhu, Q., and Zhuang, Q.: Global Methane Budget 2000–  
736 2020, *Earth Syst. Sci. Data*, 17, 1873-1958, 10.5194/essd-17-1873-2025, 2025.  
737 Schooling, C. N., Feng, L., Woodwark, A. J. P., and Palmer, P. I.: Potential of point source imaging satellite  
738 instruments to infer diffuse methane emissions: a theoretical case study of the Near-Infrared Multispectral  
739 Camera (NIMCAM), *EGUsphere*, 2026, 1-27, 10.5194/egusphere-2026-812, 2026.  
740 Sweeney, C., Chatterjee, A., Wolter, S., McKain, K., Bogue, R., Conley, S., Newberger, T., Hu, L., Ott, L.,  
741 Poulter, B., Schiferl, L., Weir, B., Zhang, Z., and Miller, C. E.: Using atmospheric trace gas vertical profiles  
742 to evaluate model fluxes: a case study of Arctic-CAP observations and GEOS simulations for the ABoVe  
743 domain, *Atmos. Chem. Phys.*, 22, 6347-6364, 10.5194/acp-22-6347-2022, 2022.  
744 Valentini, R., Arneeth, A., Bombelli, A., Castaldi, S., Cazzolla Gatti, R., Chevallier, F., Ciais, P., Grieco, E.,  
745 Hartmann, J., Henry, M., Houghton, R. A., Jung, M., Kutsch, W. L., Malhi, Y., Mayorga, E., Merbold, L.,  
746 Murray-Tortarolo, G., Papale, D., Peylin, P., Poulter, B., Raymond, P. A., Santini, M., Sitch, S., Vaglio  
747 Laurin, G., van der Werf, G. R., Williams, C. A., and Scholes, R. J.: A full greenhouse gases budget of Africa:  
748 synthesis, uncertainties, and vulnerabilities, *Biogeosciences*, 11, 381-407, 10.5194/bg-11-381-2014, 2014.  
749 van der Velde, I. R., van der Werf, G. R., van Wees, D., Schutgens, N. A. J., Vernooij, R., Houweling, S.,  
750 Tonucci, E., Chuvieco, E., Randerson, J. T., Frey, M. M., Borsdorff, T., and Aben, I.: Small Fires, Big Impact:  
751 Evaluating Fire Emission Estimates in Southern Africa Using New Satellite Imagery of Burned Area and  
752 Carbon Monoxide, *Geophysical Research Letters*, 51, e2023GL106122,  
753 <https://doi.org/10.1029/2023GL106122>, 2024.  
754 van der Werf, G. R., Randerson, J. T., Giglio, L., van Leeuwen, T. T., Chen, Y., Rogers, B. M., Mu, M., van  
755 Marle, M. J. E., Morton, D. C., Collatz, G. J., Yokelson, R. J., and Kasibhatla, P. S.: Global fire emissions  
756 estimates during 1997–2016, *Earth Syst. Sci. Data*, 9, 697-720, 10.5194/essd-9-697-2017, 2017.  
757 van der Werf, G. R., Randerson, J. T., van Wees, D., Chen, Y., Giglio, L., Hall, J., Vernooij, R., Mu, M.,  
758 Binte Shahid, S., Barsanti, K. C., Yokelson, R., and Morton, D. C.: Landscape fire emissions from the 5th  
759 version of the Global Fire Emissions Database (GFED5), *Scientific Data*, 12, 1870, 10.1038/s41597-025-  
760 06127-w, 2025.  
761 Western, L. M., Ramsden, A. E., Ganesan, A. L., Boesch, H., Parker, R. J., Scarpelli, T. R., Tunnicliffe, R.  
762 L., and Rigby, M.: Estimates of North African Methane Emissions from 2010 to 2017 Using GOSAT  
763 Observations, *Environmental Science & Technology Letters*, 8, 626-632, 10.1021/acs.estlett.1c00327, 2021.  
764 Wunch, D., Toon, G. C., Blavier, J.-F. L., Washenfelder, R. A., Notholt, J., Connor, B. J., Griffith, D. W. T.,  
765 Sherlock, V., and Wennberg, P. O.: The Total Carbon Column Observing Network, *Philosophical  
766 Transactions of the Royal Society A: Mathematical, Physical and Engineering Sciences*, 369, 2087-2112,  
767 10.1098/rsta.2010.0240, 2011.  
768 Xiao, H., Song, C., Li, S., Lu, X., Liang, M., Xia, X., and Yuan, W.: Global Wetland Methane Emissions  
769 From 2001 to 2020: Magnitude, Dynamics and Controls, *Earth's Future*, 12, e2024EF004794,  
770 <https://doi.org/10.1029/2024EF004794>, 2024.  
771 Zhang, Y., Fang, S., Chen, J., Lin, Y., Chen, Y., Liang, R., Jiang, K., Parker, R. J., Boesch, H., Steinbacher,  
772 M., Sheng, J.-X., Lu, X., Song, S., and Peng, S.: Observed changes in China's methane emissions linked to  
773 policy drivers, *Proceedings of the National Academy of Sciences*, 119, e2202742119,  
774 10.1073/pnas.2202742119, 2022.  
775 Zhou, M., Wang, Y., Duan, M., Tian, X., Ding, J., Bi, J., Ma, Y., Ma, W., and Xi, Z.: Greenhouse gas  
776 measurement campaign of the Earth Summit Mission-2022: ground-based in situ and FTIR observations and  
777 contribution to satellite validation in the Qomolangma region, *Atmos. Meas. Tech.*, 18, 4311-4324,  
778 10.5194/amt-18-4311-2025, 2025.

779